Chemical Science

ROYAL SOCIETY OF CHEMISTRY

EDGE ARTICLE

View Article Online
View Journal | View Issue

Cite this: *Chem. Sci.*, 2023, **14**, 7346

All publication charges for this article have been paid for by the Royal Society of Chemistry

Engineering the microenvironment of electron transport layers with nickle single-atom sites for boosting photoelectrochemical performance†

Ying Qin,[a] Rong Tan,[a] Jing Wen,[b] Qikang Huang,[c] Hengjia Wang,[a] Mingwang Liu,[a] Jinli Li,[a] Canglong Wang,[d] Yan Shen,[c] Liuyong Hu,*[b] Wenling Gu*[a] and Chengzhou Zhu*[a]

Received 23rd March 2023
Accepted 3rd June 2023

DOI: 10.1039/d3sc01523h

rsc.li/chemical-science

Advances in the rational design of semiconductor–electrocatalyst photoelectrodes provide robust driving forces for improving energy conversion and quantitative analysis, while a deep understanding of elementary processes remains underwhelming due to the multistage interfaces involved in semiconductor/electrocatalyst/electrolyte. To address this bottleneck, we have constructed carbon-supported nickel single atoms (Ni SA@C) as an original electron transport layer with catalytic sites of Ni–N_4 and Ni–N_2O_2. This approach illustrates the combined effect of photogenerated electron extraction and the surface electron escape ability of the electrocatalyst layer in the photocathode system. Theoretical and experimental studies reveal that Ni–N_4@C, with excellent oxygen reduction reaction catalytic activity, is more beneficial for alleviating surface charge accumulation and facilitating electrode–electrolyte interfacial electron-injection efficiency under a similar built-in electric field. This instructive method enables us to engineer the microenvironment of the charge transport layer for steering the interfacial charge extract and reaction kinetics, providing a great prospect for atomic scale materials to enhance photoelectrochemical performance.

Introduction

Semiconductor electrode-based photoelectrochemical (PEC) behavior has been broadly recognized as a promising chemical method for energy conversion[1,2] and quantitative analysis.[3–5] However, developing efficient PEC systems has been hampered by poor carrier mobility and selectivity, short carrier diffusion lengths, and sluggish electrochemical kinetics at the multistage interfaces from the semiconductor photoelectrode to electrolyte.[6–9] To suppress competing excited-carrier recombination pathways, significant effort has been devoted to developing simple and effective photoelectrodes made from light-absorbing semiconductors with electrocatalysts to improve charge separation or simply enable more facile surface reaction kinetics.[10–13] Nonetheless, the energetics and charge-transfer processes of semiconductor–electrocatalyst photoelectrodes used in PEC systems are poorly understood,[14,15] resulting from the not well-defined electrocatalysts on semiconductors.[16,17] Meanwhile, the properties of the as-synthesized photoactive materials are diverse,[18,19] with a large degree of electron–hole recombination at the photoactive material/electrocatalysts/electrolyte interfaces due to the mismatched energy band alignment.[20] To finely optimize the charge transfer process, it is a promising method to introduce a charge transfer layer that can provide an outstanding charge transfer channel at the heterojunction interface and prolong the charge trapping lifetime on the surface of the photoelectrode.[21–23]

Single-atom catalysts (SACs) involving individual and isolated metal atoms stabilized on appropriate supports have been widely studied and recognized in different fields, such as electrocatalysis,[24,25] photocatalysis,[26–29] biomimetic catalysis,[30,31] *etc.*, due to the compelling advantages of unique electronic structures, high activity, and well-defined active sites. Given the strong interaction between the metal single atom and support, regulating the local environment of single atoms that results in different electron transfer paths is expected to facilitate the extraction of photogenerated carriers from semiconductors (Interface I; charge transfer) and their injection into the electrolyte (Interface II; surface reaction).[32,33] Furthermore, the

[a]*National Key Laboratory of Green Pesticide, International Joint Research Center for Intelligent Biosensing Technology and Health, College of Chemistry, Central China Normal University, Wuhan 430079, P. R. China. E-mail: wlgu@ccnu.edu.cn; czzhu@ccnu.edu.cn*

[b]*Hubei Key Laboratory of Plasma Chemistry and Advanced Materials, School of Materials Science and Engineering, Wuhan Institute of Technology, Wuhan 430205, P. R. China. E-mail: huly@wit.edu.cn*

[c]*Wuhan National Laboratory for Optoelectronics, Huazhong University of Science and Technology, Wuhan 430074, P. R. China*

[d]*Institute of Modern Physics, Chinese Academy of Science, Lanzhou 730000, P. R. China*

† Electronic supplementary information (ESI) available. See DOI: https://doi.org/10.1039/d3sc01523h

integration of the atomically dispersed catalytic site and charge extraction layer significantly extends the charge diffusion length, establishes atomic-level charge transfer channels,[34] and enhances the electrochemical reaction driving force.[35,36] Inspired by the above analysis, it's highly desirable to obtain a deep understanding of the mechanisms for selective extraction of photoexcited minority carriers and surface reaction kinetics at the semiconductor–electrocatalyst photoelectrode, which would more generally illustrate design principles that can be applied to other material systems.

Herein, nickel-based materials are employed as an ideal model to gain a deep understanding of interface properties at the photocathode.[37–39] Thus, we decorated the electron transport layer of a carbon support with nickel single atoms (Ni SA@C) to boost the carrier dynamics of typical p-type semiconductor CuO with atomic-level charge transfer channels. Since porphyrin-like M–N_4 sites and Schiff base-like M–N_2O_2 sites in nonprecious metal SACs exhibit different electron transfer pathways for the ORR under neutral conditions, the atomic scale active centers with Ni–N_4 (Ni–N_4@C) and Ni–N_2O_2 (Ni–N_2O_2@C) also significantly affect the PEC behaviors towards CuO-based photocathodes. From the comprehensive consideration of light absorption, built-in electric field, and surface reaction energy levels, experimental investigations and theoretical calculations clarify that the electron transport process of Ni–N_4@C is much better than that of Ni–N_2O_2@C, thus achieving high-efficiency PEC performance (Scheme 1). Based on the poisoning of the active sites of Ni SA@C, we not only confirmed the importance of metal active sites on the electron transport layer to the kinetics of the solid–liquid interface reaction in the PEC system but also designed an advanced PEC biosensing platform for the sensitive detection of paraoxon. The modulation of the electron transport layer with atomically dispersed metal sites in this work furnishes in-depth insights into the PEC process, facilitating the interfacial engineering and optimization of PEC devices.

Results and discussion

Structural characterization of Ni SA@C/CuO

The electron transport layers of Ni SA@C with the active sites of Ni–N_4 and Ni–N_2O_2 were synthesized using a "ligand-mediated" method,[40,41] and the corresponding ligand structures are shown in Fig. S1.† An illustration of Ni SA@C and its integration with the semiconductor CuO for the preparation of photoelectrode materials is depicted in Fig. 1a. During the preparation, Ni SA@C was adsorbed on the surface of the CuO semiconductor by the electrostatic self-assembly method according to the measured zeta potentials in Fig. 1b. Next, the microstructure of as-synthesized Ni SA@C was characterized using transmission electron microscope (TEM) images (Fig. 1c and S2†) and X-ray diffraction (XRD) analysis (Fig. S3a†), displaying an amorphous state without the formation of Ni-related nanoparticles or clusters. Meanwhile, the selected area electron diffraction (SAED) patterns in the inset image of Fig. 1c verify the amorphous characteristics of Ni SA@C due to the weak diffraction rings. Only the diffraction peaks of CuO can be clearly recognized in the XRD result of the Ni SA@C/CuO composite (Fig. S3b and c†), which are assigned to the standard lattice planes (PDF#41-0254) of CuO. This amorphous Ni SA@C after combining with CuO was revealed by the HRTEM images (Fig. 1d) as well, discovering that Ni–N_4@C was in close contact with the (110) lattice plane of CuO. To further confirm the atomically dispersed Ni element, we performed aberration-corrected high-angle annular dark-field scanning transmission electron microscopy (AC-HAADF-STEM) measurement. The isolated bright dots were identified as Ni single atoms anchored on the carbon support (Fig. 1e and f). Thus, the subsequent theoretical model (Fig. S4†) was established based on

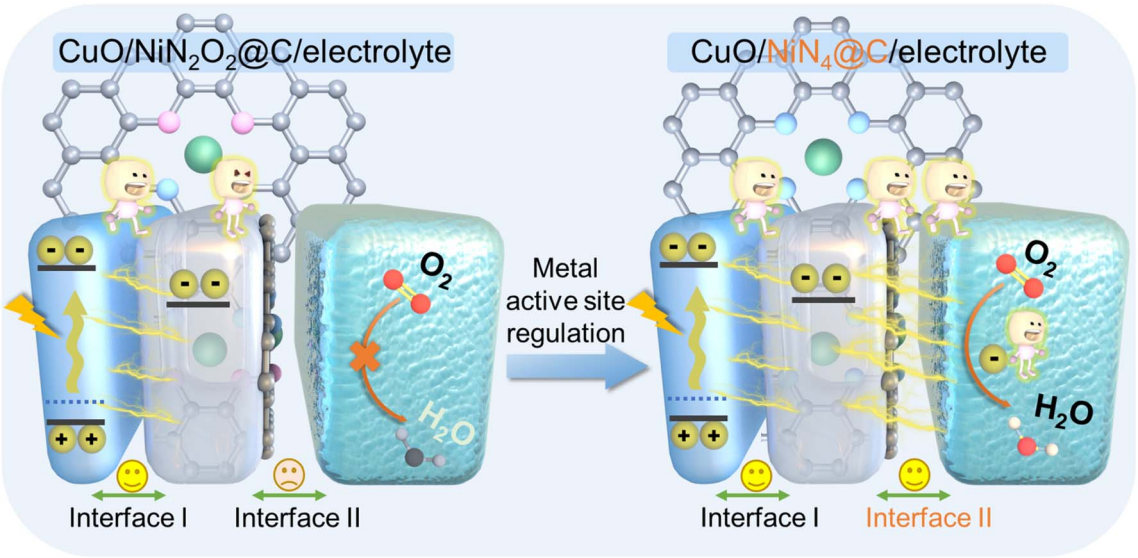

Scheme 1 Schematic diagram of the PEC process based on the regulation of metal active sites on the electron transport layer in the photocathode.

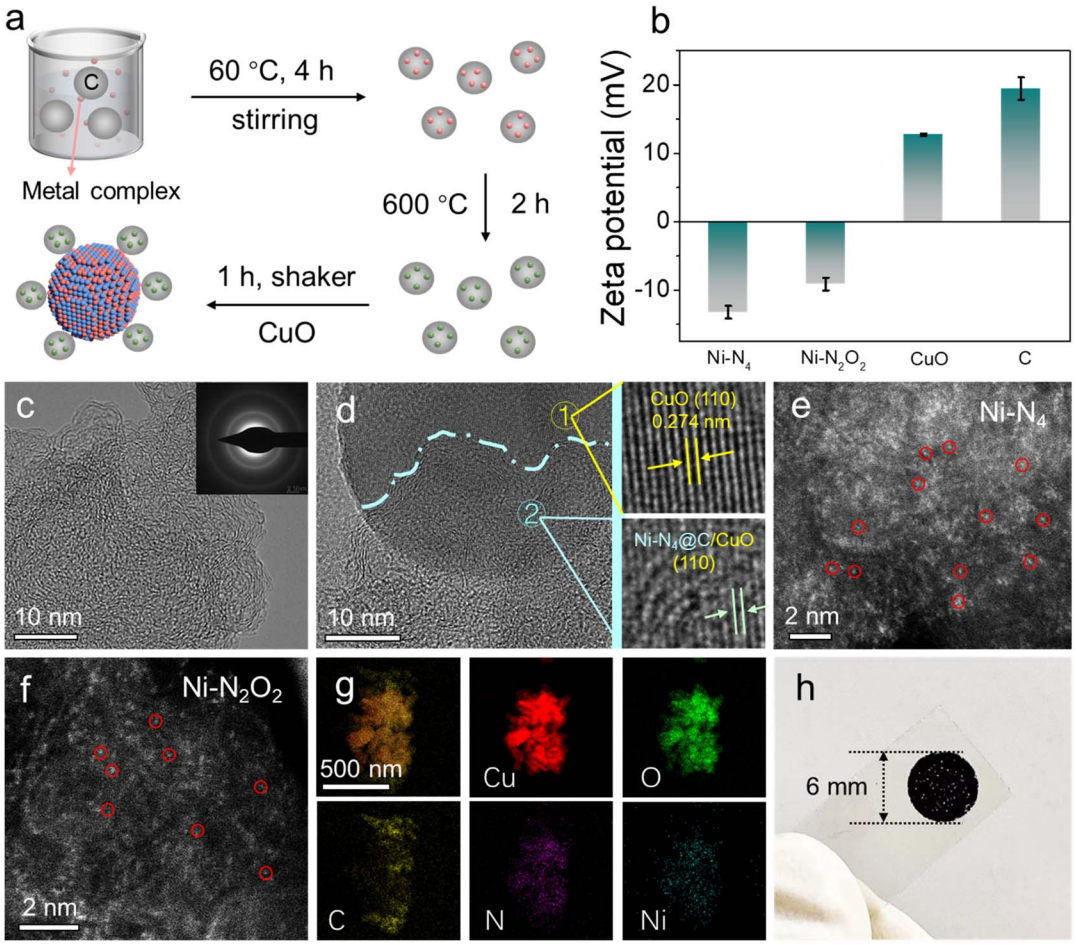

Fig. 1 (a) Schematic illustration of the synthesis process of Ni SA@C/CuO. (b) Zeta potentials of Ni–N_4@C, Ni–N_2O_2@C, CuO, and C. TEM images of (c) Ni–N_4@C (inset: SAED image) and (d) Ni–N_4@C/CuO (inset: HAADF-STEM images of CuO). AC-HADDF-STEM images of (e) Ni–N_4@C and (f) Ni–N_2O_2@C. (g) EDS mapping of Cu, O, C, N and Ni of Ni–N_4@C/CuO. (h) Photograph of the Ni–N_4@C/CuO modified electrode.

the exposed crystal facet and single atomic structure. The corresponding energy-dispersive spectroscopy (EDS) element mapping images of Ni–N_4@C/CuO also show that the C, Cu, O, N, and Ni elements are uniformly distributed in the composite (Fig. 1g). To identify the surface element composition and chemical states of Ni SA@C, CuO, and Ni SA@C/CuO, X-ray photoelectron spectroscopy (XPS) was employed. As presented in Fig. S5a,† C, Cu, O, N, and Ni elements can be detected in the Ni SA@C/CuO composite, which are in accordance with the EDS results. The binding energies were calibrated against the C–C peak in C 1s spectra at 284.8 eV (Fig. S6b†). As for O 1s (Fig. S5b†) and Cu 2p (Fig. S6a†) spectra of different samples, it could be clearly noticed that the binding energy had a positive shift in Ni–N_4@C/CuO and Ni–N_2O_2@C/CuO. In contrast, the binding energies of Ni–N_4@C/CuO and Ni–N_2O_2@C/CuO show obvious negative shifts in N 1s (Fig. S6c†) and Ni 2p (Fig. S6d†) spectra. The opposite charge transfer indicates a strong interfacial interaction between CuO and Ni SA@C. Moreover, in the spectra of C 1s and O 1s, the characteristic peak of the C–O bond increases in the composite samples,[42,43] indicating the chemically bonded C–O interface between CuO and catalysts. Finally, the prepared Ni SA@C/CuO was modified on the photoelectrode unit, which adopted a circular area size with a uniform radius of 3 mm to support PEC testing (Fig. 1h).

General PEC performances and basic photoelectric properties of Ni SA@C/CuO

The systematic research on photocurrent transients of the Ni SA@C/CuO photocathodes under 100 mW cm^{-2} simulated sunlight illumination in PBS solution (pH = 7.4) is plotted in Fig. 2a and S7.† In comparison to bare CuO, temporal measurements of Ni–N_2O_2@C/CuO, C/CuO, and Ni–N_4@C/CuO modified photoelectrodes in photocurrent are enhanced by 1.4, 2.1, and 3.1 times, respectively, pointing to the favorable charge transfer or surface reaction ability after loading Ni SA@C on semiconductors. The current–voltage characteristics of modified photoelectrodes were studied through the linear sweep voltammetry (LSV) curves in Fig. 2b under continuous and on–off cycle illumination. When the p-type semiconductor CuO was modified with the Ni–N_4@C-based electron transport layer, the photocurrent density can reach a value of 1.19 mA cm^{-2} at −0.1 V (*vs.* Ag/AgCl) with a remarkable onset potential (E_{onset}) of 0.2 V, which significantly exceed the performance of bare CuO. This

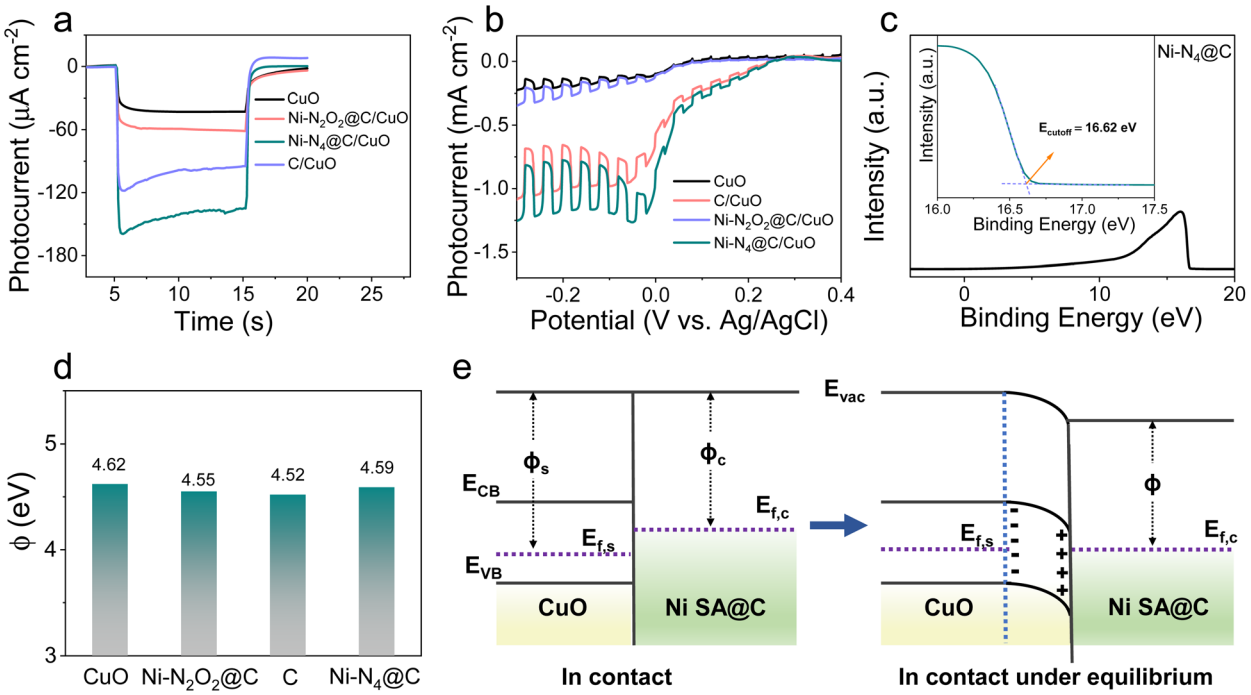

Fig. 2 (a) Photocurrent responses for CuO, Ni–N_2O_2@C/CuO, C/CuO, and Ni–N_4@C/CuO. (b) LSV of CuO, Ni–N_2O_2@C/CuO, C/CuO, and Ni–N_4@C/CuO. (c) UPS spectra of Ni–N_4@C. (d) Work function comparison of CuO, Ni–N_2O_2@C, C, and Ni–N_4@C. (e) Energy band diagrams of the catalyst and p-type semiconductor CuO contacts. E_{vac}, vacuum energy; E_{CB}, energy of the conduction band minimum; E_{VB}, energy of the valence band maximum; ϕ_s, CuO work function; ϕ_c, Ni SA@C work function.

increment in the photocurrent could be attributed to the passivation of electron–hole pair recombination, which is closely related to the extraction of photogenerated electrons in CuO and the accelerated photo-excited ORR kinetics.

Ultraviolet-visible (UV-vis) diffuse reflectance spectra were first examined to disclose their optical absorption properties. As presented in Fig. S8,† the band gap energy (E_g) values of CuO, Ni–N_2O_2@C/CuO, C/CuO, and Ni–N_4@C/CuO are determined from the Tauc plot of $(\alpha h\nu)^2$ *vs.* energy ($h\nu$), hovering around 1.47 eV. The virtually unchanged E_g proves that Ni SA@C does not change the light-absorption performance of CuO itself. At the same time, the Ni SA@C alone has almost no photocurrent response (Fig. S9†), which also implies that Ni SA@C has no light energy conversion function and the generation of photocarriers mainly comes from CuO. Then, we studied their solid-state electronic properties to understand the electron extraction ability of such electron transport layers for semiconductor CuO. The surface energetics of Ni SA@C and CuO were investigated by ultraviolet photoelectron spectroscopy (UPS) (Fig. 2c and S10†), and the work functions (ϕ) of CuO, Ni–N_2O_2@C, C, and Ni–N_4@C are determined to be about 4.62, 4.55, 4.52 and 4.59 eV, respectively (Fig. 2d). The work function of Ni SA@C (ϕ_c) is smaller than that of CuO (ϕ_s), being $\phi_s > \phi_c$ in Fig. 2e, and then the band of CuO will bend downward forming a space charge layer until their Fermi levels (E_f) reach an equilibrium.[44] As a result, the built-in electric field in the space charge layer of CuO is directed from the surface into the inside of the semiconductor. Thus, once the electron–hole pairs are generated in Ni SA@C/CuO, the photoelectrons are extracted to the Ni SA@C pole, which facilitates the separation of carriers in the CuO semiconductor. In terms of the strength of the formed built-in electric field, Ni–N_2O_2@C and Ni–N_4@C will exhibit similar electron extraction abilities at the semiconductor/catalyst interface due to similar E_f. Then, three-dimensional (3D) charge density differences (Fig. S11†) were calculated to reveal the interlayer charge transfer between the CuO (110) and Ni SA@C. As expected, the Ni SA@C could induce electron depletion on CuO (110) through the Mülliken charge analysis ($\delta_{e,\ Ni\ SA@C} < 0$, −1.61 e for Ni–$N_4$@C and −1.63 e for Ni–$N_2O_2$@C). Likewise, the charge accumulation values in Ni–N_2O_2@C and Ni–N_4@C areas confirm the ability to extract electrons from the semiconductor CuO, but the difference was not significant. The results of the steady-state photoluminescence spectra also confirm this phenomenon, showing few differences in the quenching effect of the electron–hole pair recombination in all-solid-state Ni–N_4@C/CuO and Ni–N_2O_2@C/CuO (Fig. S12†). To figure out the essence of the Ni–N_4@C electron transport layer with the greatest influence on the PEC signal, we shift our attention to the perspective of electron exchange at the solid–liquid interface regardless of little difference in solid-state physical electronic properties (Ni–N_4@C ≈ Ni–N_2O_2@C).

Working mechanism characterization of PEC behavior at the solid–liquid interface

The electrochemical ORR properties of Ni–N_2O_2@C, Ni–N_4@C, and C were first examined in O_2-saturated 0.1 M PBS at room temperature, and a strong ORR peak was observed for each catalyst in cyclic voltammetry (CV) curves, denoting their eximious interfacial catalytic activity (Fig. S13a†). Concurrently,

ORR polarization curves for Ni SA@C were further recorded on the rotating ring-disk electrode (RRDE) (Fig. S13b†). The Ni–N_4@C layer offers the highest ORR current and the most positive onset potential, suggesting that the Ni–N_4@C layer has the best ORR catalytic activity among the tested samples (Ni–N_4@C > C > Ni–N_2O_2@C). Meanwhile, the average electron-transfer number and peroxide yield percentage of the samples (Fig. S13c and d†) are calculated. As a result, the average electron transfer number of Ni–N_4@C is higher than that of C and Ni–N_2O_2@C, indicating that Ni–N_4@C favors an apparent $4e^-$ ORR process with low H_2O_2 yield. Subsequently, electrochemical ORR tests (Fig. 3a) were performed on the CuO electrodes integrated with the Ni SA@C to illustrate the reaction kinetics of the solid–liquid interface. The results prove that the interfacial ORR properties of different composites are improved, and the tendency of ORR activity remains unchanged after adding CuO (Ni–N_4@C/CuO > C/CuO > Ni–N_2O_2@C/CuO). This ORR capacity trend demonstrates that the local atomic environments of metal Ni sites induced by ligands play an important role in catalytic activity, which will in turn determine the electrode–electrolyte interfacial electron-injection efficiency. Besides, LSV curves of samples in different atmosphere-saturated electrolytes (O_2 and N_2) were obtained under dark and light conditions. As expected, the photocurrent of Ni–N_4@C/CuO in the N_2-saturated electrolyte cannot hold a candle to that in the O_2-saturated electrolyte, demonstrating that the extra transfer of photoelectrons in the electron extraction layer can be enhanced due to the ORR activity at the solid–liquid interface (Fig. 3b). Compared with Ni–N_4@C/CuO, C/CuO and Ni–N_2O_2@C/CuO with inferior ORR efficiency exhibit limited photocurrent (Fig. S14†), which verifies the critical influence of Ni SA@C structures on the photoelectron consumption rate of the photocathode surface as well. Moreover, density functional theory (DFT) calculations were carried out to gain fundamental insight into the electron transport differences of the Ni SA@C/CuO (110) for oxygen molecules, and the results are depicted in Fig. 3c and d. The

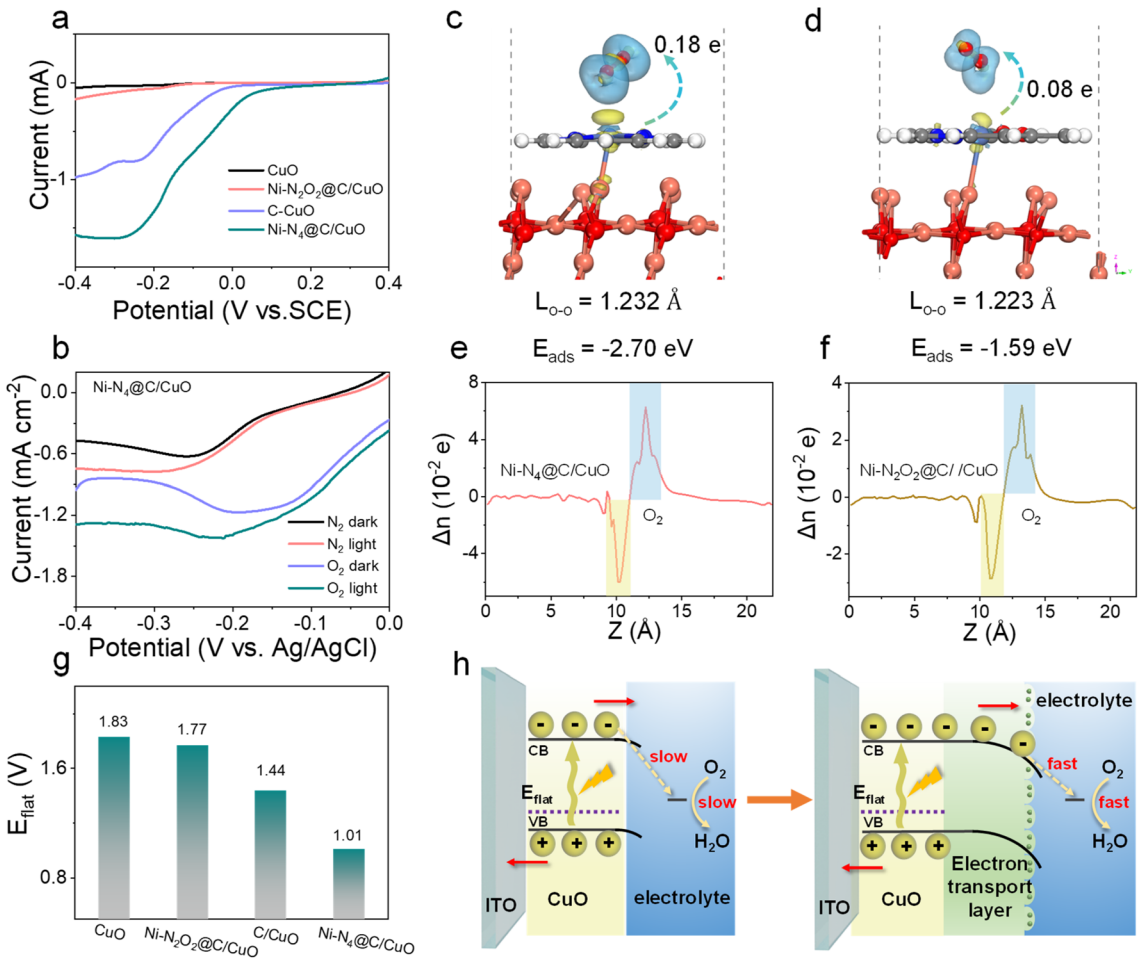

Fig. 3 (a) The ORR polarization curves of CuO, Ni–N_2O_2@C/CuO, C/CuO, and Ni–N_4@C/CuO in 0.1 M PBS (pH = 7.4). (b) LSV (with and without light) of Ni–N_4@C/CuO in the O_2 and N_2 saturated-buffer electrolyte, respectively. Theoretical calculation of O_2 adsorption and the side view of the charge density difference on (c) Ni–N_4@C/CuO and (d) Ni–N_2O_2@C/CuO. Planar-averaged electron density difference Δn (z) for (e) Ni–N_4@C/CuO and (f) Ni–N_2O_2@C/CuO. The transferred electron was determined by Mülliken charge calculations. The blue and yellow isosurfaces depict charge accumulation and depletion in the space, respectively. The positive values and the negative values indicate electron accumulation and electron depletion, respectively. (g) Flat band potential comparison of CuO, Ni–N_2O_2@C/CuO, C/CuO, and Ni–N_4@C/CuO. (h) Solid–liquid interface energy band diagrams of the photocathode.

adsorption energy for oxygen molecules on the Ni–N_4@C/CuO (110) surface (−2.70 eV) is significantly stronger than that on the Ni–N_2O_2@C/CuO (110) surface (−1.59 eV), suggesting that Ni–N_4 sites are more favorable to enhance the activation of O_2 during the interfacial reaction. Thereupon, the bond length of oxygen molecules on the Ni–N_4@C/CuO (110) surface (1.232 Å) is stretched to a greater extent compared with the Ni–N_2O_2@C/CuO (110) surface (1.223 Å). The Mülliken charge of oxygen molecule ($\delta_{e,\ oxygen} < 0$) analyses also supports the fact that Ni–N_4@C/CuO (110) could induce more electron transfer from the surface to the oxygen molecule, being −0.18 e for O_2|Ni–N_4@C/CuO (110) and −0.08 e for O_2|Ni–N_2O_2@C/CuO (110). Meanwhile, the planar-averaged charge density differences (Fig. 3e and f) of O_2|Ni–N_4@C/CuO (110) and O_2|Ni–N_2O_2@C/CuO (110) along the *Z* direction were analyzed according to the 3D charge density differences, signifying that electrons are more able to slide impulsively from the Ni–N_4@C/CuO side to the O_2 side across the interface. To further explore the PEC behavior of the photocathode/solution interface, flat band potentials (E_{flat}) were measured by the Mott–Schottky (M–S) technique at 1000 Hz in PBS solution (pH = 7.4) (Fig. S15† and 3g). After modifying these electron transport layers on CuO, the E_{flat} values of the samples have negative intercept shifts, especially for Ni–N_4@C/CuO. According to previous studies,[45–47] the negative shift of the E_{flat} of the system indicates the rise of the E_f (Ni–N_4@C/CuO > C/CuO > Ni–N_2O_2@C/CuO > CuO), leading to the energy band bending down in the PEC cell. The elevated energy level values of the electron transport layer/CuO photocathodes confirm that the electrons in the Ni–N_4@C/CuO conduction band are more likely to react with O_2 in PBS solution with a larger driving force. Additionally, typical electrochemical impedance spectroscopy (EIS) Nyquist plots of the as-prepared samples are illustrated in Fig. S16.† The arc diameter in Nyquist plots for the Ni–N_4@C/CuO sample was largely reduced, meaning the easier charge transfer at the solid–liquid interface. As described in the schematic diagram (Fig. 3h), the driving force for the surface ORR is enhanced by this outstanding electron transport layer with excellent catalytic site activity and electron extraction ability.

Furthermore, we took advantage of electron paramagnetic resonance (EPR) with the spin labeling technique to evaluate the reduction behavior of photoelectrons in the samples. 2,2,6,6-Tetramethylpiperidine-1-oxyl (TEMPO) can be reduced by photoelectrons into hydroxyl amine, TEMPOH, accompanied by quenching of the EPR signal.[48] Therefore, TEMPO was used to probe the reactivity of electrons generated in photoexcited CuO and Ni SA@C/CuO (Fig. 4a). The EPR spectrum of TEMPO exhibits three peaks with an intensity of 1 : 1 : 1, and the intensity was almost unchanged after mixing with samples before irradiation (Fig. S17†). However, the signal intensity of TEMPO in the mixed solution decreased rapidly after 2 min of irradiation, indicating that the photoelectron reduces spin-labeled TEMPO to an EPR silencing product. The greatest decline in EPR signal intensity was found for C/CuO and Ni–N_4@C/CuO, where more photoelectrons are exchanged for the photo-reduction reaction. To further uncover how the surface photoelectron reaction kinetics influence the PEC performance, scanning electrochemical microscopy (SECM) characterization in feedback mode was performed on the CuO and Ni SA@C/CuO samples. The molecular probe of $[Fe(CN)_6]^{4-}$ was first oxidized at the Pt ultramicroelectrode (UME) (E_T = 0.6 V *vs.* Ag/

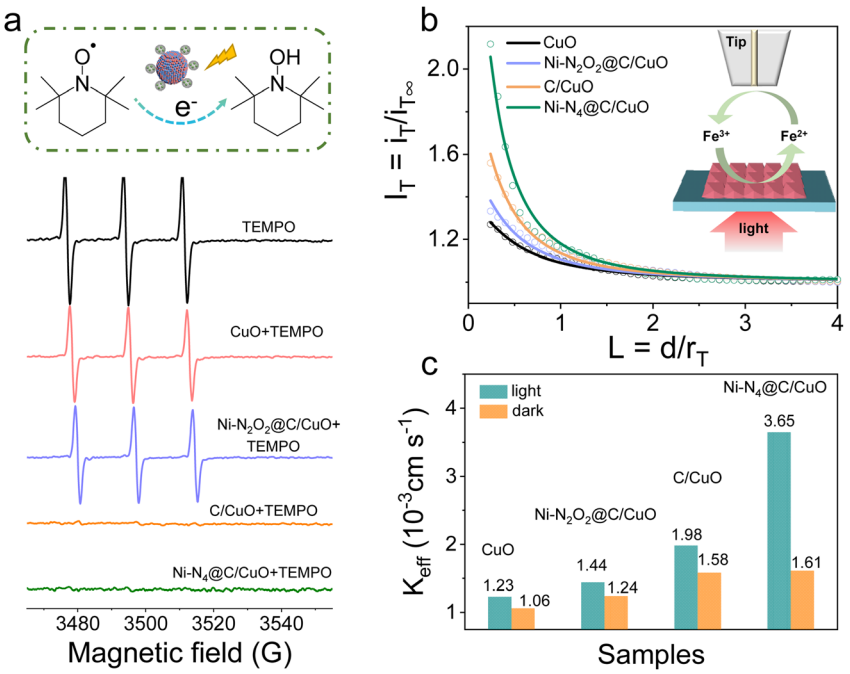

Fig. 4 (a) EPR spectra at room temperature of the samples containing 0.03 mM TEMPO in the absence and presence of CuO, Ni–N_2O_2@C/CuO, C/CuO, and Ni–N_4@C/CuO. All the spectra were recorded at 2 min during irradiation. (b) Normalized SECM approach curves in the feedback mode with the Pt UME approaching different samples with the redox mediator 2 mM $[Fe(CN)_6]^{4-}$ under illumination, r_T = 12.5 μm. (c) Rate constant (K_{eff}) of different samples under light and dark conditions.

AgCl) to generate $[Fe(CN)_6]^{3-}$. The formed $[Fe(CN)_6]^{3-}$ diffuses to the photocathode surface and subsequently reacts with the photoelectrons.[49,50] Fig. 4b presents the probe approach curves (I_T–L curves) of the samples under illumination, among which Ni–N_4@C/CuO has the largest positive feedback current. In contrast, the approach curves without illumination show poor feedback effects, demonstrating the promotion effect of photoelectrons (Fig. S18†). In addition, the effective heterogeneous charge transfer rate constant (k_{eff}) can be gained by data fitting (Table S1†) and plotted in Fig. 4c. From the above results, k_{eff} manifests an increasing trend of Ni–N_4@C/CuO > C/CuO > Ni–N_2O_2@C/CuO > CuO. The solid–liquid interfacial charge transfer rate of Ni–N_4@C/CuO is about 2.4 times higher than that of Ni–N_2O_2@C/CuO, which means that the modulation of the surface charge transfer pathway plays a beneficial role in promoting reaction kinetics.

PEC biosensing properties based on Ni–N_4@C/CuO

Based on the above research, we applied this Ni SA@C/CuO photocathode to the detection of paraoxon, an acetylcholinesterase (AChE) inhibitor. Thiocholine, the enzymolysis product of acetylthiocholine (ATCh), can effectively poison Ni single-atom sites, resulting in a slow surface reaction kinetics of the photoelectrode. First, to study the sensitivity of different electrode materials to thiocholine molecules, we calculated the charge density differences of Ni–N_4@C/CuO (110) and Ni–N_2O_2@C/CuO (110) to simulate the interaction between surface active sites and sulfhydryl molecules. As displayed in Fig. 5a, Ni–N_4@C/CuO (110) reflects a stronger charge transfer process and adsorption performance. As a result, the photocurrent changes of the four samples were also observed after being poisoned with thiocholine (Fig. 5b). Interestingly, Ni–N_4@C/CuO was seriously poisoned by the sulfhydryl molecule with a noticeable decrease in photocurrent. The order of ability in being poisoned is Ni–N_4@C/CuO > Ni–N_2O_2@C/CuO > C/CuO ≈ CuO, which is in accordance with the theoretical calculations. Hence, we selected the optimized Ni–N_4@C/CuO materials to monitor the concentration of paraoxon. The Ni–N_4@C/CuO with a feed ratio of 7.4% Ni–N_4@C reflects the best photocurrent (Fig. S19 and Table S2†). In addition, the concentrations of the enzyme and substrate were finally selected as 500 mU mL^{-1} and 1 mM according to the optimization results (Fig. S20†). Under optimized experimental conditions, the I–t curves of the fabricated photocathode incubated with different concentrations of paraoxon are illustrated in Fig. 5c. The photocurrent linearly increased with the logarithm of paraoxon concentrations from 0.03 to 50 ng mL^{-1}, and the linear regression equation (Fig. 5d) can be given by $I = 4.792 \lg C + 9.882$ ($R^2 = 0.996$) with a limit of detection (LOD) of 0.02 ng mL^{-1} (signal-to-noise ratio of 3). The as-prepared PEC sensing platform also expresses good selectivity to different interfering species, including, Na^+, Zn^{2+}, Mg^{2+}, ascorbic acid (AA), glycine, vitamin E (VE), glucose, and bovine serum albumin (BSA) (Fig. S21†). Besides, the developed Ni SA@C/CuO photocathode demonstrates better PEC stability under consecutive on–off light irradiation for 300 s in comparison with the bare CuO (Fig. S22†), which can be ascribed to the weakened redox peak of CuO after loading Ni SA@C for the prevention of photo corrosion (Fig. S23†). Finally, the reliability and practicability of the PEC sensing platform were evaluated in the paraoxon-adsorbed real samples of cucumber, tomato, apple, and cabbage. The recovery rates are in the range of 90.00–110.5% with the relative standard deviations ranging from 1.56 to 7.25% (Table S3†), which is in accordance with the results

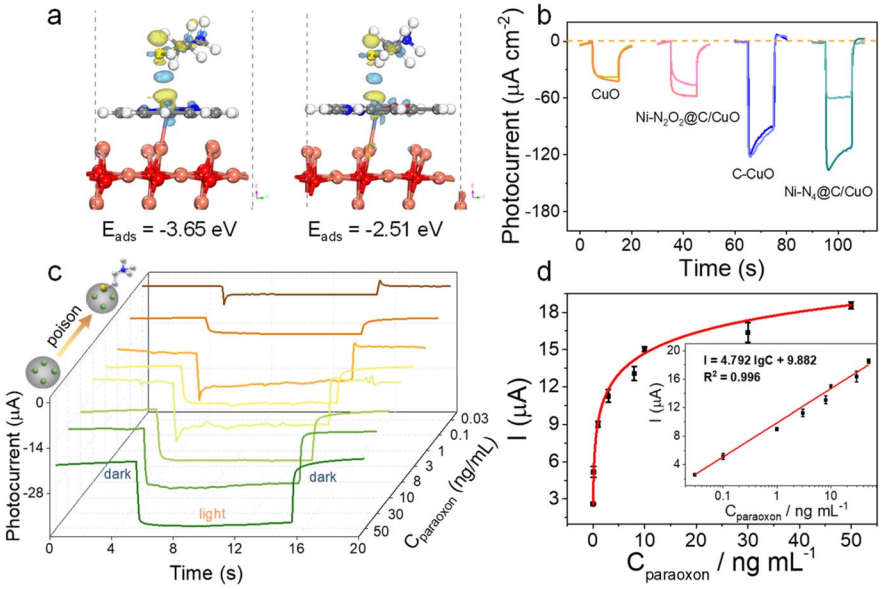

Fig. 5 (a) Theoretical calculation of sulfhydryl molecule adsorption on (left) Ni–N_4@C/CuO (110) and (right) Ni–N_2O_2@C/CuO (110). (b) Photocurrent response comparison of CuO, Ni–N_2O_2@C/CuO, C/CuO, and Ni–N_4@C/CuO after the poisoning. (c) Photocurrent responses of Ni–N_4@C/CuO/ITO with different concentrations of paraoxon. (d) Calibration curve of the Ni–N_4@C/CuO-based PEC sensor within the range of 0.03–50 ng mL^{-1} for paraoxon.

measured by gas chromatography (Fig. S24†), implying potential application in practical sample analysis.

Conclusions

In summary, we have developed an innovative coupling method to regulate atomically dispersed catalytic sites (Ni–N_4 and Ni–N_2O_2) on electron transport layers for the interpretation of carrier dynamics in semiconductor/electrocatalyst/electrolyte interfaces. The atomic design of active centers on electron transport layers offers a modulated surface energy structure for electron extraction and a favorable charge transfer channel for facilitated activation of reactants, thus enhancing PEC stability and responsivity. In comparison to Ni–N_2O_2@C, the modification of p-type semiconductor CuO with the Ni–N_4@C electron transport layer greatly reduces the barriers to photoelectron migration and the surface ORR, achieving the best photocurrent response. Thanks to this outstanding electron transport layer, a sensitive and quantitative PEC assay of paraoxon was successfully realized using the as-prepared Ni–N_4@C/CuO photocathode. The demonstrated charge transport layer design strategy opens an avenue for facilitating charge transfer and accelerating surface reaction kinetics by the construction of atomically dispersed catalytic sites.

Data availability

The data that support the findings of this study are available in the ESI† of this article.

Author contributions

Ying Qin: investigation, data Curation, writing-original draft. Rong Tan: providing help in measurements. Jing Wen: theoretical calculation. Qikang Huang: scanning electrochemical microscopy analysis. Hengjia Wang: formal analysis. Mingwang Liu: validation. Jinli Li: validation. Canglong Wang: theoretical calculation. Yan Shen: scanning electrochemical microscopy analysis. Liuyong Hu: supervision, conceptualization, writing-review & editing. Wenling Gu: supervision, methodology, formal analysis. Chengzhou Zhu: supervision, funding acquisition, writing-review & editing, project administration.

Conflicts of interest

There are no conflicts to declare.

Acknowledgements

The authors gratefully acknowledge the financial support from the National Natural Science Foundation of China (no. 22104114), the Natural Science Foundation of Hubei Province (2021CFB518), the Fundamental Research Funds for the Central Universities (no. CCNU22JC006), and the Program of Introducing Talents of Discipline to Universities of China (111 program, B17019).

Notes and references

1 D. E. Scaife, *Sol. Energy*, 1980, **25**, 41–54.
2 M.-H. Ham, J. H. Choi, A. A. Boghossian, E. S. Jeng, R. A. Graff, D. A. Heller, A. C. Chang, A. Mattis, T. H. Bayburt, Y. V. Grinkova, A. S. Zeiger, K. J. Van Vliet, E. K. Hobbie, S. G. Sligar, C. A. Wraight and M. S. Strano, *Nat. Chem.*, 2010, **2**, 929–936.
3 W.-W. Zhao, J.-J. Xu and H.-Y. Chen, *Chem. Soc. Rev.*, 2015, **44**, 729–741.
4 R. Saran and R. J. Curry, *Nat. Photonics*, 2016, **10**, 81–92.
5 S. Cestellos-Blanco, H. Zhang, J. M. Kim, Y.-X. Shen and P. Yang, *Nat. Catal.*, 2020, **3**, 245–255.
6 Q. Wang and K. Domen, *Chem. Rev.*, 2020, **120**, 919–985.
7 Y.-F. Xu, H.-S. Rao, B.-X. Chen, Y. Lin, H.-Y. Chen, D.-B. Kuang and C.-Y. Su, *Adv. Sci.*, 2015, **2**, 1500049.
8 R. A. Pala, A. J. Leenheer, M. Lichterman, H. A. Atwater and N. S. Lewis, *Energy Environ. Sci.*, 2014, **7**, 3424–3430.
9 C. Li, Z. Luo, T. Wang and J. Gong, *Adv. Mater.*, 2018, **30**, 1707502.
10 S. M. Thalluri, L. Bai, C. Lv, Z. Huang, X. Hu and L. Liu, *Adv. Sci.*, 2020, **7**, 1902102.
11 F. Lin and S. W. Boettcher, *Nat. Mater.*, 2014, **13**, 81–86.
12 X. Ning, P. Du, Z. Han, J. Chen and X. Lu, *Angew. Chem., Int. Ed.*, 2021, **60**, 3504–3509.
13 G. Zhao, Y. Sun, W. Zhou, X. Wang, K. Chang, G. Liu, H. Liu, T. Kako and J. Ye, *Adv. Mater.*, 2017, **29**, 1703258.
14 L. Li, X. Yang, Y. Lei, H. Yu, Z. Yang, Z. Zheng and D. Wang, *Chem. Sci.*, 2018, **9**, 8860–8870.
15 G. M. Carroll and D. R. Gamelin, *J. Mater. Chem. A*, 2016, **4**, 2986–2994.
16 M. R. Nellist, F. A. L. Laskowski, F. Lin, T. J. Mills and S. W. Boettcher, *Acc. Chem. Res.*, 2016, **49**, 733–740.
17 J. R. Hemmerling, A. Mathur and S. Linic, *Adv. Energy Mater.*, 2022, **12**, 2103798.
18 D. V. Esposito, I. Levin, T. P. Moffat and A. A. Talin, *Nat. Mater.*, 2013, **12**, 562–568.
19 N. Zhang, M.-Q. Yang, Z.-R. Tang and Y.-J. Xu, *ACS Nano*, 2014, **8**, 623–633.
20 L. An and H. Onishi, *ACS Catal.*, 2015, **5**, 3196–3206.
21 X. Ning, B. Lu, Z. Zhang, P. Du, H. Ren, D. Shan, J. Chen, Y. Gao and X. Lu, *Angew. Chem., Int. Ed.*, 2019, **58**, 16800–16805.
22 K. Wang, Y. Liu, K. Kawashima, X. Yang, X. Yin, F. Zhan, M. Liu, X. Qiu, W. Li, C. B. Mullins and J. Li, *Adv. Sci.*, 2020, **7**, 2002563.
23 T. A. Pham, Y. Ping and G. Galli, *Nat. Mater.*, 2017, **16**, 401–408.
24 M. B. Gawande, K. Ariga and Y. Yamauchi, *Small*, 2021, **17**, 2101584.
25 S. Sultan, J. N. Tiwari, A. N. Singh, S. Zhumagali, M. Ha, C. W. Myung, P. Thangavel and K. S. Kim, *Adv. Energy Mater.*, 2019, **9**, 1900624.
26 C. Gao, J. Low, R. Long, T. Kong, J. Zhu and Y. Xiong, *Chem. Rev.*, 2020, **120**, 12175–12216.
27 X. Li, W. Bi, L. Zhang, S. Tao, W. Chu, Q. Zhang, Y. Luo, C. Wu and Y. Xie, *Adv. Mater.*, 2016, **28**, 2427–2431.

28 P. Zhou, M. Luo and S. Guo, *Nat. Rev. Chem.*, 2022, **6**, 823–838.
29 J. N. Tiwari, A. N. Singh, S. Sultan and K. S. Kim, *Adv. Energy Mater.*, 2020, **10**, 2000280.
30 Y. Wu, W. Xu, L. Jiao, W. Gu, D. Du, L. Hu, Y. Lin and C. Zhu, *Chem. Soc. Rev.*, 2022, **51**, 6948–6964.
31 W. Xu, L. Jiao, Y. Wu, L. Hu, W. Gu and C. Zhu, *Adv. Mater.*, 2021, **33**, 2005172.
32 C. Ding, J. Shi, Z. Wang and C. Li, *ACS Catal.*, 2017, **7**, 1706.
33 S. Chen, S. Shen, G. Liu, Y. Qi, F. Zhang and C. Li, *Angew. Chem., Int. Ed.*, 2015, **54**, 3047–3051.
34 F. Chen, T. Ma, T. Zhang, Y. Zhang and H. Huang, *Adv. Mater.*, 2021, **33**, 2005256.
35 X. Bai, X. Zhao, Y. Zhang, C. Ling, Y. Zhou, J. Wang and Y. Liu, *J. Am. Chem. Soc.*, 2022, **144**, 17140–17148.
36 X. Wei, S. Song, W. Cai, X. Luo, L. Jiao, Q. Fang, X. Wang, N. Wu, Z. Luo, H. Wang, Z. Zhu, J. Li, L. Zheng, W. Gu, W. Song, S. Guo and C. Zhu, *Chem*, 2023, **9**, 181–197.
37 V. Vij, S. Sultan, A. M. Harzandi, A. Meena, J. N. Tiwari, W.-G. Lee, T. Yoon and K. S. Kim, *ACS Catal.*, 2017, **7**, 7196–7225.
38 S. Liu, H. B. Yang, S.-F. Hung, J. Ding, W. Cai, L. Liu, J. Gao, X. Li, X. Ren, Z. Kuang, Y. Huang, T. Zhang and B. Liu, *Angew. Chem., Int. Ed.*, 2020, **59**, 798–803.
39 R. Anand, A. S. Nissimagoudar, M. Umer, M. Ha, M. Zafari, S. Umer, G. Lee and K. S. Kim, *Adv. Energy Mater.*, 2021, **11**, 2102388.
40 H. Yang, L. Shang, Q. Zhang, R. Shi, G. I. N. Waterhouse, L. Gu and T. Zhang, *Nat. Commun.*, 2019, **10**, 4585.
41 Y. Wang, R. Shi, L. Shang, G. I. N. Waterhouse, J. Zhao, Q. Zhang, L. Gu and T. Zhang, *Angew. Chem., Int. Ed.*, 2020, **59**, 13057–13062.
42 M. Zhang, M. Lu, Z.-L. Lang, J. Liu, M. Liu, J.-N. Chang, L.-Y. Li, L.-J. Shang, M. Wang, S.-L. Li and Y.-Q. Lan, *Angew. Chem., Int. Ed.*, 2020, **59**, 6500–6506.
43 M. Zhang, X. Wang, H. Sun, N. Wang, J. He, N. Wang, Y. Long, C. Huang and Y. Li, *ACS Cent. Sci.*, 2020, **6**, 950–958.
44 Z. Zhang and J. T. Yates Jr, *Chem. Rev.*, 2012, **112**, 5520–5551.
45 V. Subramanian, E. E. Wolf and P. V. Kamat, *J. Am. Chem. Soc.*, 2004, **126**, 4943–4950.
46 M. Sun and X. Cui, *Electrochem. Commun.*, 2012, **20**, 133–136.
47 A. I. Kontos, V. Likodimos, T. Stergiopoulos, D. S. Tsoukleris, P. Falaras, I. Rabias, G. Papavassiliou, D. Kim, J. Kunze and P. Schmuki, *Chem. Mater.*, 2009, **21**, 662–672.
48 W. He, H. Jia, W. G. Wamer, Z. Zheng, P. Li, J. H. Callahan and J.-J. Yin, *J. Catal.*, 2014, **320**, 97–105.
49 Z. Yu, Q. Huang, X. Jiang, X. Lv, X. Xiao, M. Wang, Y. Shen and G. Wittstock, *Anal. Chem.*, 2021, **93**, 12221–12229.
50 G. Wittstock, M. Burchardt, S. E. Pust, Y. Shen and C. Zhao, *Angew. Chem., Int. Ed.*, 2007, **46**, 1584–1617.